Numerical Heat Transfer, Part A, 39:433–448, 2001

1040-7782/01 $12.00 + .00

EFFECT OF INCLINED VORTEX GENERATORS ON HEAT TRANSFER ENHANCEMENT IN A THREE-DIMENSIONAL CHANNEL

Ahmad Sohankar and Lars Davidson
Department of Thermo and Fluid Dynamics, Chalmers University of Technology, SE-412 96, Göteborg, Sweden

Three-dimensional unsteady flow and heat transfer in a channel with inclined block shape vortex generators mounted on one side of a channel flow are investigated for different Reynolds numbers, $\mathbf{Re}_H = \mathbf{400-1500}$***, and*** $\mathbf{Pr} = \mathbf{0.71}$***. This study was informed to gain an understanding of the flow phenomena and calculate the heat transfer and pressure drop for different Reynolds numbers. The effect of computational domain, angle of incidence, size of the vortex generator, and the discretization schemes on the results are also investigated. Simulations use an incompressible finite volume code, based on a fractional step technique with a multigrid pressure Poisson solver and a nonstaggered grid arrangement.***

INTRODUCTION

The subject of heat transfer enhancement is relevant to the design of more compact and less expensive heat exchangers with high energy performance. Compact heat exchangers are used in power and process industrial applications, such as the automotive industry and air-conditioning, electronic cooling, spacecraft, and aircraft applications. Different mechanisms such as the creation of electric or acoustic fields, surface vibration, fluid additive, and use of a special surface geometry may be employed for heat transfer enhancement, which can be classified into two groups: main flow and secondary flow enhancement [1]. The mechanisms of these different methods often are based on creating developing boundary layers, swirl or vortices, and stimulating flow destabilization or turbulence intensification [2–4]. One common method widely used for heat transfer enhancement is to employ heat transfer surfaces that are periodically interrupted along the streamwise direction. Some typical examples of such surfaces are louvered fin, offset fin, offset strip fin, and rectangular plate fin [5–11]. Another common method for enhancing heat transfer is to apply vortex generators such as fins, ribs, wings, and so on [2–4, 12]. The vortex generators are special surfaces that are used to generate secondary flow or vortices by swirling and destabilizing the flow. In addition, these vortices have a tendency to last for

Received 16 June 2000; accepted 20 October 2000.
This research is a part of an EU project, the Vortex Enhanced Heat Exchangers (VEHE) project. Funding for this work by the EU Commission through contract JOE3CT970056 is gratefully appreciated.
Address correspondence to L. Davidson, Department of Thermo and Fluid Dynamics, Chalmers University of Technology, SE-412 96 Göteborg, Sweden.

NOMENCLATURE

a_P	diagonal coefficient in the discretized equation	t	time
a_P^o	coefficient in the discretized equation (time derivative)	T	temperature
a_{nb}	neighbor coefficients $(a_W, a_E, \ldots)$ in discretized equation	U, V, W	Cartesian velocity components in x, y and z direction, respectively
B	width of computation domain (see Figure 1)	x_o	distance between leading edge of vortex generator and inlet (see Figure 1)
b	source term in the discretized equation or thickness of vortex generator (see Figure 1)	x, y, z	Cartesian coordinates (streamwise, wall-normal and spanwise, see Figure 1)
H	height of channel	VG	vortex generator
h	height of vortex generator (see Figure 1)	α	underrelaxation factor or convection heat transfer coefficient
l	length of vortex generator (see Figure 1)	β	angle of incidence (see Figure 1)
L	length of computation domain (see Figure 1)	Δt	time step
P	pressure	θ	dimensionless temperature
Pr	Prandtl number ν/α	ν	kinematic vixcosity
Re	Reynolds number $U_o H/\nu$	ρ	density
S	source term in the discretized equation	**Subscripts**	
		o	inlet
		w	wall

a long period and to have small cores, allowing an influence on heat transfer over long and narrow regions [4]. The vortex generators can generate transverse or longitudinal vortices depending on the geometry and angle of attack of the vortex generators.The axis of transverse vortices (also called spanwise or primary vortices) is perpendicular to the main flow direction. These types of vortices are generated from flow separation and unstable shear layers, and the flow can remain two-dimensional. The Karman vortex street in the wake of bluff bodies, e.g., circular and rectangular cylinders, is one known example of transverse vortices [13–15]. The longitudinal vortices (streamwise or secondary vortices) are induced by vortex generators causing the flow to swirl around the axis parallel to the main flow. This type of vortices, which always produces three-dimensional flow, can also be observed in the wake of bluff bodies at $\mathrm{Re} \approx 200$ [15–17]. Different types of vortex generators, such as rectangular and triangular wings and winglets, have been considered for channel flows; see, e.g., [4, 12, 18]. In general, longitudinal vortices are more efficient than transverse vortices for heat transfer enhancement. In addition, longitudinal vortices enhance heat transfer locally and globally in steady flow, while transverse vortices generate a negligible global heat transfer enhancement in steady flow [4].

The main objective of this numerical study is to investigate effects of a pair of blocks as vortex generators, which are mounted on one side of a channel, for different Reynolds numbers, $\mathrm{Re}_H = 400-1500$, and $\mathrm{Pr} = 0.71$. This geometry is similar to that studied in [19]. This study was made to gain an understanding of the flow phenomena and to calculate the heat transfer and pressure losses for different

Reynolds numbers. The effects of computational domain, angle of incidence, size of the vortex generator, and the discretization schemes on the results are also investigated.

PROBLEM DESCRIPTION

As shown in Figure 1, the physical problem considered in this study is the three-dimensional flow of an incompressible fluid passing over two inclined blocks, which are used as vortex generators (VG). The flow is described in a coordinate system (x, y, z) in which the x-axis is aligned with the inflow, streamwise direction, the z-axis is in the spanwise direction and the y-axis is perpendicular to both x and z; see Figure 1. Two three-dimensional vortex generators are mounted on one side of the horizontal channel with an angle of incidence, β, to the streamwise direction, x-axis. The height (y direction) of the channel and the vortex generators is denoted by H and h, respectively. An incompressible flow with constant fluid properties is assumed. The Reynolds number is defined as $\mathrm{Re} = U_o H/\nu$, where U_o is the constant inflow velocity. All geometrical lengths are scaled with H. Velocities are scaled with U_o, and physical time is scaled with H/U_o. The dimensionless temperature is defined as $\theta = (T - T_o)/(T_w - T_o)$, where T_w is the constant temperature at the channel walls and vortex generators and T_o is a constant inflow temperature. The pressure is scaled with ρU_o^2, where ρ is the density.

COMPUTATIONAL DETAILS

An incompressible finite volume code based on a fractional step technique and employing a nonstaggered grid arrangement was used. The scheme was implicit in time, and a second-order Crank–Nicolson scheme was used. All terms except the convective term were discretized using the second-order central differencing

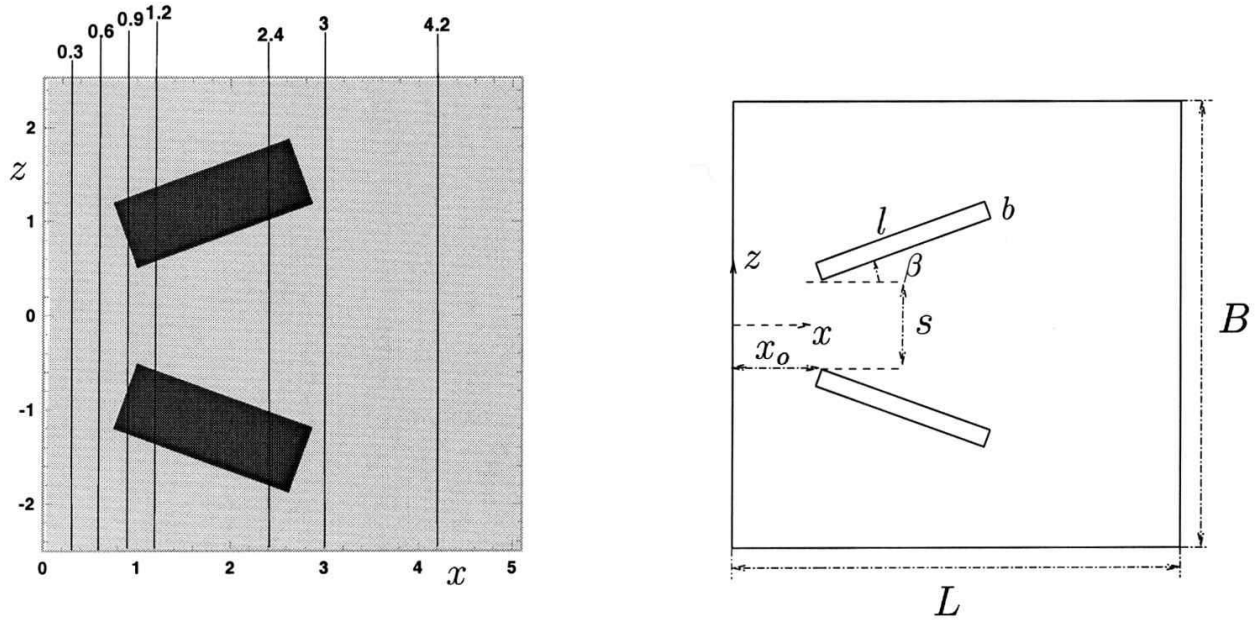

Figure 1. Schematic drawing of the computatonal domain.

scheme. The convective term was discretized using either the second-order central or the third-order QUICK differencing scheme. It should be noted that the QUICK scheme is third-order accurate in one-dimensional discretization. In multi-dimensional flow, as in the present case, the formal overall accuracy is only second order. In practice, however, QUICK is more accurate than second-order schemes. It should furthermore be noticed than the formal order of the schemes (both the central scheme and the QUICK scheme) deteriorates when the grid is stretched. If the stretching is kept at reasonable levels (below 10%), this does not have any noticeable impact on the results. It could also be mentioned that when refining the grid the stretching is reduced if the refinement is done properly.

The time-marching calculations were started with the fluid at rest, and a constant dimensionless time step, $\Delta t = 0.01$, was used. During the iterative sequence, convergence was assessed at the end of each iteration on the basis of the residual sources criterion, which compares the sum of the absolute residual source over all the control volumes in the computational field, for each finite volume equation. The residuals for the continuity, momentum, and temperature equations were normalized with the incoming mass flux, momentum flux, and convective energy flux, respectively. The convergence criterion was set to 0.001 and was usually reached after two outer iterations. The distance from the VG surface to the nearest grid point was set at ≈ 0.01 for all calculations in this study. The hyperbolic tangent function was used for stretching, see Figure 2. A uniform grid between nodes was used in the y direction.

Uniform flow ($U = 1$, $V = W = \theta = 0$) was prescribed at the inlet. At the outlet, the convective boundary condition ($\partial U/\partial t + U_o \partial u/\partial x = 0$) was used for the streamwise velocity component. The Neumann condition was used for V, W, and θ at the outlet. No-slip conditions were prescribed at the VG surfaces, the lower ($y = 0$) and upper ($y = H$) walls of the channel. The nondimensional temperature was set to $\theta = 1$ on the VGs and channel walls, where $T = T_w$. Symmetry

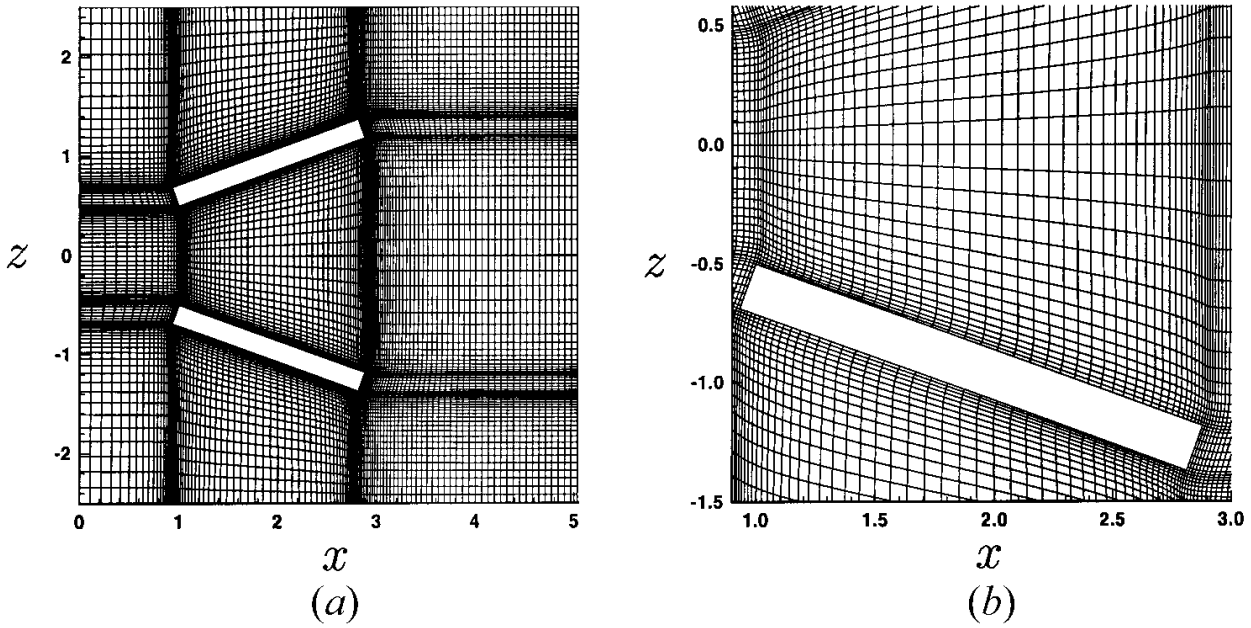

Figure 2. Grid in $x-z$ plane (113 × 97, Cases 5 and 6; see Table 1). (*a*) Whole domain, (*b*) close-up of grid around vortex generator.

conditions ($\partial U/\partial z = \partial V/\partial z = \partial\theta/\partial z = W = 0$) were used in the spanwise direction. The normal derivative for the pressure was set to zero at all boundaries. Computational parameters are listed for six cases in Table 1. Simulations were carried out for different Reynolds numbers ($\mathrm{Re}_H = 400, 1000, 1500$) for each case.

METHOD OF SOLUTION

The continuity, Navier–Stokes, and energy equations in dimensionless form for incompressible flow with constant fluid properties are as follows:

$$\frac{\partial U_i}{\partial x_i} = 0 \tag{1}$$

$$\frac{\partial U_i}{\partial t} + \frac{\partial}{\partial x_j}(U_i U_j) = -\frac{\partial P}{\partial x_i} + \frac{1}{\mathrm{Re}}\frac{\partial^2 U_i}{\partial x_j \partial x_j} \tag{2}$$

$$\frac{\partial \theta}{\partial t} + \frac{\partial}{\partial x_i}(U_i\theta) = \frac{1}{\mathrm{Re}\,\mathrm{Pr}}\frac{\partial^2\theta}{\partial x_i \partial x_i}, \qquad \theta = \frac{T - T_o}{T_w - T_o} \tag{3}$$

An incompressible finite volume code with a nonstaggered grid arrangement was used. After discretization, Eqs. (1), (2), and (3) were solved with an implicit fractional step method. All terms in the momentum (2) and energy (3) equations were advanced in time using the Crank–Nicolson scheme [20], as follows:

$$U_i^{n+1} = U_i^n + \Delta t\, H(U_i^n, U_i^{n+1}) - \alpha\Delta t\,\frac{\partial P^{n+1}}{\partial x_i} - (1-\alpha)\Delta t\frac{\partial P^n}{\partial x_i} \tag{4}$$

$$\theta^{n+1} = \theta^n + \Delta t\, H((\theta U_i)^n,\ (\theta U_i)^{n+1}) \tag{5}$$

where superscripts n and $n+1$ denote old and new time levels, respectively, and $H(U_i^n, U_i^{n+1})$ and $H((\theta U_i)^n, (\theta U_i)^{n+1})$ include the convection and diffusion terms, that is,

$$\begin{aligned} H(U_i^n, U_i^{n+1}) = {} & \alpha\mathrm{Re}^{-1}\frac{\partial^2 U^{n+1}}{\partial x_j \partial x_j} + (1-\alpha)\mathrm{Re}^{-1}\frac{\partial^2 U^n}{\partial x_j \partial x_j} \\ & - \alpha\frac{\partial}{\partial x_j}\left(U_i^{n+1}U_j^{n+1}\right) - (1-\alpha)\frac{\partial}{\partial x_j}\left(U_i^n U_j^{n+1}\right) \end{aligned} \tag{6}$$

Table 1. Summary of dimensionless computatonal parameters. H and h are the channel wall spacing and the height of the vortex generators, respectively; see Figure 1. "C" and "Q" denote CENTRAL and QUICK scheme, respectively.

Case	Grid	L	B	l	b	x_o	s	H	b	β	Scheme
1	$121 \times 33 \times 97$	6	5	2	0.2	2	1	1	0.5	**10**	C
2	$121 \times 33 \times 97$	6	5	2	0.2	2	1	1	0.5	**20**	C
3	$121 \times 33 \times 97$	6	5	2	0.2	2	1	1	0.5	**30**	C
4	$121 \times 33 \times 97$	6	5	2	**0.5**	2	1	1	0.5	20	C
5	$113 \times 33 \times 97$	5	5	2	0.2	**1**	1	1	0.5	20	C
6	$113 \times 33 \times 97$	5	5	2	0.2	**1**	1	1	0.5	20	**Q**

$$H((\theta U_i)^n, (\theta U_i)^{n+1}) = \alpha(\mathrm{Re\,Pr})^{-1}\frac{\partial^2\theta^{n+1}}{\partial x_j\partial x_j} + (1-\alpha)(\mathrm{Re\,Pr})^{-1}\frac{\partial^2\theta^n}{\partial x_j\partial x_j} - \alpha\frac{\partial}{\partial x_j}\left((\theta U_j)^{n+1}\right) - (1-\alpha)\frac{\partial}{\partial x_j}(U_j^{n+1}\theta^n) \tag{7}$$

In this study α was set to 0.6.

The numerical solution procedure for obtaining U_i and P, θ at each time step can be summarized as follows.

1. Solve the discretized Eq. (4), employing a symmetric Gauss–Seidel solver, for obtaining U_i^{n+1}. For example, the standard form of the U equation ($i = 1$) is

$$a_P U_P^{n+1} = \sum a_{nb} U_{nb}^{n+1} + b \tag{8}$$

where

$$\begin{aligned} b &= (1-\alpha)\sum a_{nb} U_{nb}^n + \left[a_P^o - (1-\alpha)\sum a_{nb}\right]U_P^n + S \\ a_P^o &= (\Delta t)^{-1}\delta V \quad (\ \delta\mathrm{V} \text{ is the control volume}) \\ a_P &= a_P^o + \alpha\sum a_{nb} \end{aligned} \tag{9}$$

The gradients of pressure in Eq. (4) (levels n and $n+1$) are put in the source term (S). At this stage, the most recent values of pressure and velocities are used to obtain U_i^{n+1}.

2. Intermediate velocities are defined as

$$U_i^* = U_i^n + \Delta t\, H(U_i^n, U_i^{n+1}) - (1-\alpha)\Delta t\,\frac{\partial P^n}{\partial x_i} \tag{10}$$

Using Eq. (4), we can calculate U_i^* as

$$U_i^* = U_i^{n+1} + \alpha\Delta t\,\frac{\partial P^{n+1}}{\partial x_i} \tag{11}$$

The intermediate velocity field (U_i^*) does not satisfy the continuity equation. Velocities at control volume faces (U_{face}^*) are calculated by interpolation from neighboring intermediate velocities at nodes. These interpolated cell face velocities are used to calculate the mass fluxes and convection fluxes.

3. To satisfy continuity for $U_{i(\mathrm{face})}^{n+1}$, take the divergence of Eq. (11) and insert $\partial U_{i(\mathrm{face})}^{n+1}/\partial x_i = 0$; thus

$$\frac{\partial^2 P^{n+1}}{\partial x_i\partial x_i} = (\alpha\Delta t)^{-1}\,\frac{\partial U_{i(\mathrm{face})}^*}{\partial x_i} \tag{12}$$

This is the Poisson equation for obtaining pressure on level ($n+1$). This equation is solved with a multigrid Poisson solver [21].

4. The cell face velocities are corrected. For example, the U component ($i = 1$) is written as

$$U_{\text{face}}^{n+1} = U_{\text{face}}^{*} - \alpha \Delta t \left(\frac{\partial P^{n+1}}{\partial x} \right) \Bigg|_{\text{face}} \tag{13}$$

These velocities are used to calculate the mass fluxes at faces of the control volume that are used to satisfy the continuity equation.

5. Solve the discretized Eq. (5) for obtaining θ^{n+1}. This equation is solved in the same way as in stage 1.

Stages 1–5 are carried out for each iteration until a global convergence criterion for the continuity, momentum, and energy equations at each time step is fulfilled.

RESULTS AND DISCUSSION

Three-dimensional unsteady flow in a channel with a pair of three-dimensional vortex generators, mounted on one side of a channel, were performed for different Reynolds numbers, $\mathrm{Re}_H = 400-1500$, and $\mathrm{Pr} = 0.71$. Quantities such as normalized instantaneous temperature, $\theta = (T - T_o)/(T_w - T_o)$, and pressure and velocity field were calculated during a long simulation period. The local Nusselt number is defined with a local temperature gradient at the wall as

$$\mathrm{Nu}(x, z) = \frac{\alpha(x, z) H}{k} = -\frac{\partial \theta}{\partial y} \Bigg|_{\text{wall}} \tag{14}$$

where $\alpha(x, z)$ and k are the local convection heat transfer coefficient and conduction heat transfer coefficient, respectively.

The spanwise-averaged Nusselt number, $\mathrm{Nu}(x)$, and surface-averaged Nusselt number, Nu, are defined as

$$\mathrm{Nu} = \frac{\int \mathrm{Nu}(x, z)\, dz}{\int dz} \tag{15}$$

$$\mathrm{Nu} = \frac{\int\int \mathrm{Nu}(x, z)\, dz\, dx}{\int\int dz\, dx} \tag{16}$$

In this study, the cross-sectional average pressure, $P(x)$, bulk temperature, $\theta_b(x)$, and apparent friction factor, f, were computed on the basis of the following formulas:

$$P(x) = \frac{\int\int P(x, y, z)\, dz\, dy}{\int\int dz\, dy} \tag{17}$$

$$\theta_b(x) = \frac{\int\int \theta(x, y, z) u(x, y, z)\, dz\, dy}{\int\int u(x, y, z) dz\, dy} \tag{18}$$

$$f = \frac{\Delta P}{0.5 \rho U_o^2} \frac{A_o}{A} \tag{19}$$

where A_o and A are the cross-sectional area and total surface area, respectively. Note that all quantities are dimensionless values, as mentioned in the section "Problem Description."

Steady and Unsteady Flow

By considering the time evolution of velocity components and the temperature at different chosen points of the calculation domain, the simulations indicated that the flow is steady up to $\mathrm{Re}_H = 1000$ and that unsteady flow occurs at a higher Reynolds number, $\mathrm{Re}_H > 1000$, for all cases except Case 6, see Figure 3. As mentioned in Table 1, the convective term was discretized using the second-order central scheme for Cases 1–5 and the QUICK differencing scheme for Case 6. In Figure 3 it is seen that flow becomes steady for all Reynolds numbers in Case 6. This is because the QUICK scheme is dissipative and damps out all fluctuations for this low Reynolds number. It is well known that in unsteady flow simulations, non-dissipative schemes should be used [22, 23]. Dissipative schemes are useful in steady computations where they reduce numerical oscillations. However, in unsteady simulations dissipative schemes reduce not only numerical oscillations, but also the physical ones.

The unsteadiness is large around the body, in the wake and separation regions, and downstream of the vortex generators, but these effects are negligible upstream of the vortex generators. Although the exact Reynolds numbers at which the flow becomes unsteady are not calculated in this study, these values depend on the geometrical parameters of the vortex generators. For example, it is observed that there is a slight unsteadiness at a higher angle of incidence ($\beta = 30$, Case 3) at $\mathrm{Re}_H = 1000$, whereas for the other cases the flow is steady at this Reynolds number. In general, the onset of unsteadiness occurs between Reynolds numbers 1000 and 1500 for all cases.

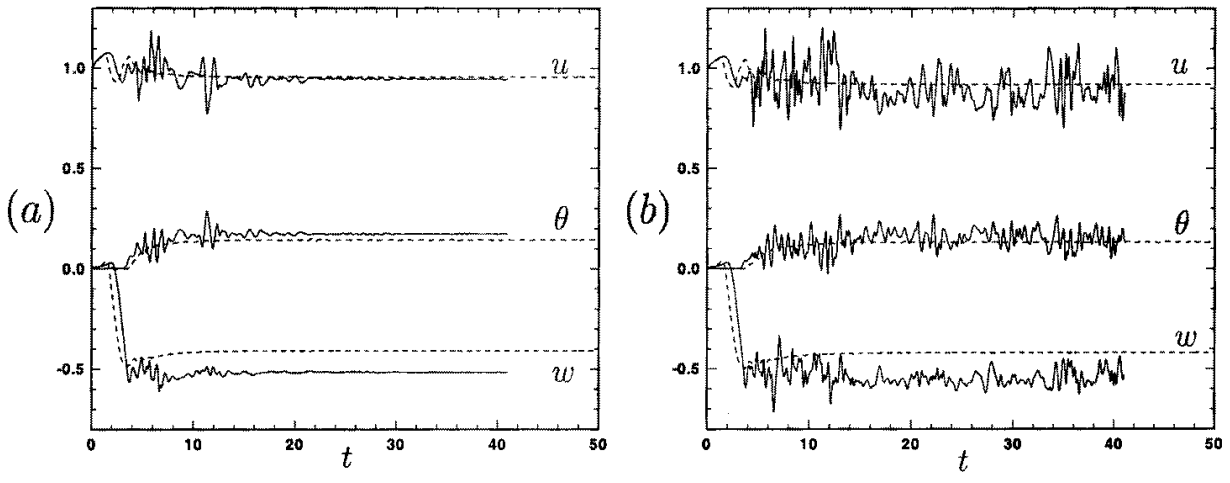

Figure 3. Time evolution of velocity components (U, W) and temperature (θ) at a chosen point ($x = 5$, $y = 0.22$, $z = -1.13$). QUICK scheme (Case 6): dashed line; CENTRAL scheme (Case 5): solid line. (a) $\mathrm{Re} = 1000$, (b) $\mathrm{Re} = 1500$.

Heat and Fluid Flow Structures

This type of flow, in spite of its relatively simple geometry, is complex and contains many complex phenomena, such as separation, recirculation, wake flow, and attached and curved free shear layers. Some of these phenomena are observed in Figures 4 and 5 for $\mathrm{Re}_H = 400$ and $\mathrm{Re}_H = 1500$. The time-averaged streamlines are presented for Case 4. As is seen in Figure 4, the VGs induce a high-speed region at the lower channel wall, which bends around the VGs in a horseshoe pattern. This is especially visible for the high Reynolds number (Figure 4*b*). As is seen in this figure, heat transfer is enhanced in the high-speed region (the horseshoe).

The sharp corners of the VGs are natural locations of separation; see Figures 4 and 5. Figures 5*a* and 5*b* show time-averaged streamlines in two streamwise planes. The positions of the $x = 3.8$ and $x = 5.8$ are close to the downstream part of the VGs (the trailing edge) and close to the outlet of the computational domain, respectively. As is seen in Figure 5*a*, the flow separates from the outer upper corners and reattachment points appear on the upper surface close to the opposite (inner) upper corners. Separations also occur at the inner edges, close to the upper corners, inducing two strong streamwise vortices close to the inner sides of the bodies. At around $x = 4$ (the trailing edge of the VGs), the vortices on the upper and inner sides detach, merge together, and move into the wake downstream of the bodies; see Figure 5*b* at position $x = 5.8$. These streamwise vortices have a low pressure in the core section with an elliptic shape. This distortion of the cross section from a circular to an elliptical shape and the skewness of the vortex core are caused by interaction of these streamwise vortices with the upper and lower channel walls during the formation and shedding process. These vortices induce a flow toward and away from the lower wall, which enhances the mixing of cold and hot fluid. The downwash secondary flow is responsible for heat transfer enhancement. The upwash movement increases the thickness of the thermal layer, which decreases the heat transfer (Nusselt number). However,the upwash regions coincide with the high-speed region of the form of horseshoe vortices mentioned above

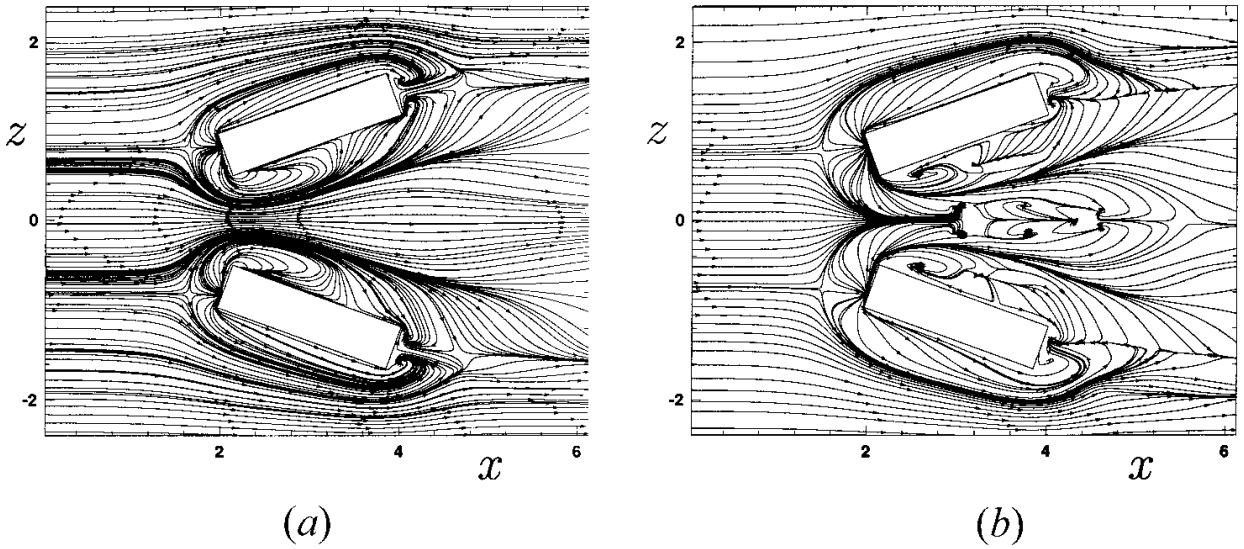

Figure 4. Time-averaged surface streamlines, Case 4. (*a*) $\mathrm{Re}_H = 400$, (*b*) $\mathrm{Re}_H = 1500$.

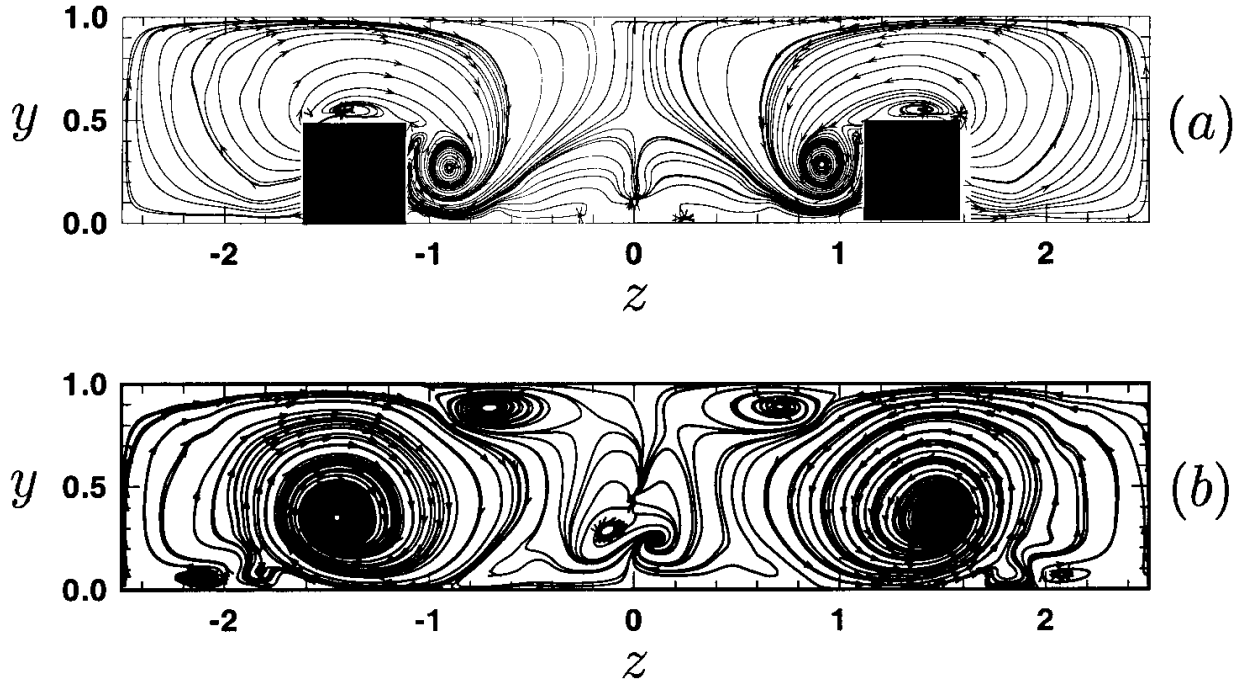

Figure 5. Time-averaged streamlines. Case 4. $\mathrm{Re}_H = 1500$. (*a*) $x = 3.8$, (*b*) $x = 5.8$.

(Figure 4*b*), and the total effect is an increase in Nusselt number, which can be seen from Figure 6*a*.

The pair of large vortices at $z \simeq \pm 1.4$ downstream from the VGs (see Figure 5*b*) induces another two pairs of vortices, one pair close to the upper wall at $z \simeq \pm 0.7$, and one pair of small vortices closeto the lower wall at $z \simeq \pm 2.1$. The sense of rotation of these two pairs of vortices is opposite to that of the pair of large vortices at $z \simeq \pm 1.4$.

Parametric Studies

This study also investigated the effects of computational domain, angle of incidence, size of the vortex generator, and the discretization schemes on the results; see Table 1. In the parametric studies, Case 2 is the baseline case and it is changed by one parameter in each case except Case 6, in which two parameters are changed in comparison to Case 2. These parameters are indicated by bold-faced values in Table 1. Please note that for emphasis, some figures (e.g., see Figures 7–9) refer to parameters of β and b (bold-faced value in Table 1) instead of case number.

Influence of Reynolds number and angle of incidence. The effect of the angle of incidence between $\beta = 10^\circ$ and $\beta = 30^\circ$ was studied for different Reynolds numbers, $\mathrm{Re}_H = 400-1500$.

The contours of the local Nusselt numbers at the lower channel wall and VG surfaces are shown in Figure 6. Please note that the instantaneous local Nusselt number is shown in Figure 6*c*, while the other plots in this figure are the time-averaged local Nusselt number. As is seen, in front of the VG, the local Nusselt numbers are high. These values increase for increasing Reynolds numbers. For example, the maximum time-averaged local Nusselt numbers in front of the

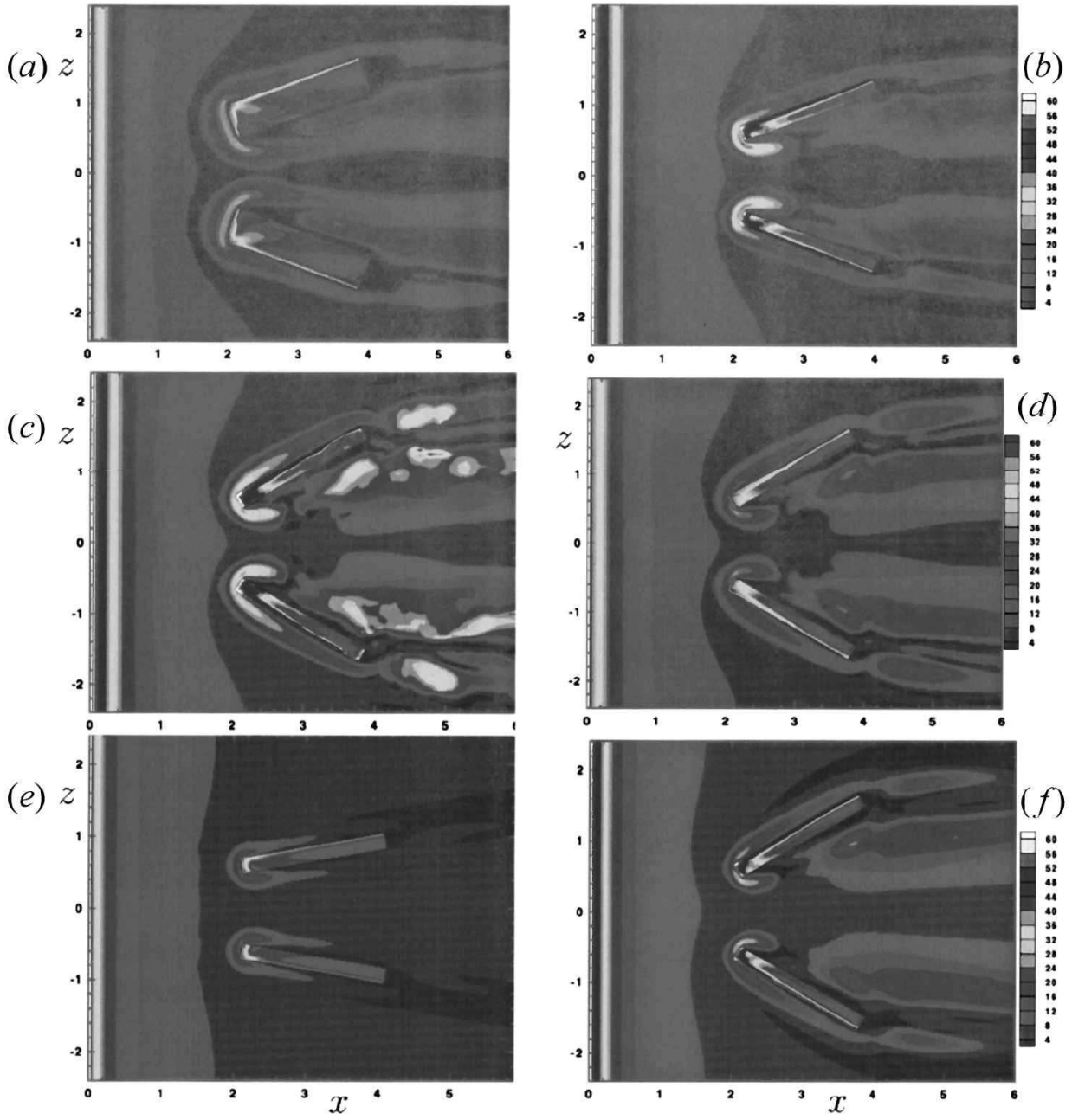

Figure 6. Local Nusselt number, $\mathrm{Nu}(x, z)$, contours on the lower channel wall and VG surfaces. (*a*) $\mathrm{Re}_H = 1500$, Case 4; (*b*) $\mathrm{Re}_H = 1500$, Case 2; (*c*) $\mathrm{Re}_H = 1500$, Case 3 (instantaneous); (*d*) $\mathrm{Re}_H = 1500$, Case 3; (*e*) $\mathrm{Re}_H = 1000$, Case 1; (*f*) $\mathrm{Re}_H = 1000$, Case 3. Note that plot (*c*) shows the instantaneous values at one time instant, whereas the other plots are time averaged.

VGs are about 14 and 38 for Reynolds numbers 400 and 1500, respectively, for Case 2. Furthermore, local Nusselt numbers on the upper side of the VGs are high, especially at the leading and outer corners of the VGs. Downstream of the VGs, where the streamwise vortices are active, the local Nusselt numbers are high. The maximum time-averaged value of $\mathrm{Nu}(x, z)$ in this region is about 30 for $\mathrm{Re} = 1500$ (Case 2), see Figure 6. The instantaneous local Nusselt numbers at one time instant for Case 3 are shown in Figure 6*c*. If we compare this figure with Figure 6*d*, which is time averaged, the values of $\mathrm{Nu}(x, z)$ upstream of the VGs are similar, with a negligible unsteadiness in instantaneous values in comparison with the time-averaged values. Most of the differences between instantaneous

and time-averaged local Nusselt numbers are observed in the wake region and downstream of the VGs, where the streamwise vortices are active. As mentioned earlier, unsteadiness is also higher in these regions. By increasing the angle of incidence from 10° to 30°, the local Nusselt numbers sharply increase as does the strength of streamwise vortices in the wake region downstream of the VGs. This causes the heat transfer enhancement to change in time-averaged and local values; see Figures 6*e* and 6*f* for $\mathrm{Re} = 1000$.

In Figure 7, the variations of time- and area-averaged Nusselt number and friction factor, which are normalized with the corresponding values in fully developed channel flow, are shown for Cases 1–4. As is seen, the Nu and f increase for increasing Reynolds numbers and also angle of incidence from 10° to 30° (Cases 1–3). By increasing the angle of incidence from 10° to 30°, the difference between the values of Nu and f increases for increasing Reynolds numbers, although these differences are higher for f then for Nu. For example, when β is increased from 10° to 30°, the increased values for Nu and f are 6.8% and 30%, respectively, at $\mathrm{Re}_H = 400$, while they are 13.5% and 50% at $\mathrm{Re}_H = 1500$. When Re_H is increased from 400 to 1500, the increased values for Nu and f are 90% and 108%, respectively, at $\beta = 20$, whereas they are 100% and 132% at $\beta = 30$. Similar trends are also observed in Figure 8, where variations in the time- and spanwise-averaged Nusselt number in the streamwise direction are shown for different Reynolds numbers and angles of incidence. The variation of Nusselt number with angle of incidence shown in Figure 8 agrees well with the predictions presented in Ref. [24]. The variations in $\mathrm{Nu}(x)$ at each Reynolds number for these three angles of incidence are approximately similar in the region upstream of the VGs, but the dissimilarity of $\mathrm{Nu}(x)$ increases with increasing angle of incidence and Reynolds numbers in the position of the VGs (approximately between $x = 2$ and $x = 4$) and downstream of the VGs. As is seen in Figure 8, the level of $\mathrm{Nu}(x)$ increases with increasing Re_H at all angles of incidence. In all of these curves, there are peaks in the level of $\mathrm{Nu}(x)$ in front of the vortex generators ($x \simeq 2$). After this peak and along the VGs (approximately between $x = 2$ and $x = 4$), the level of $\mathrm{Nu}(x)$ gradually decreases and reaches an approximately constant level for all cases except

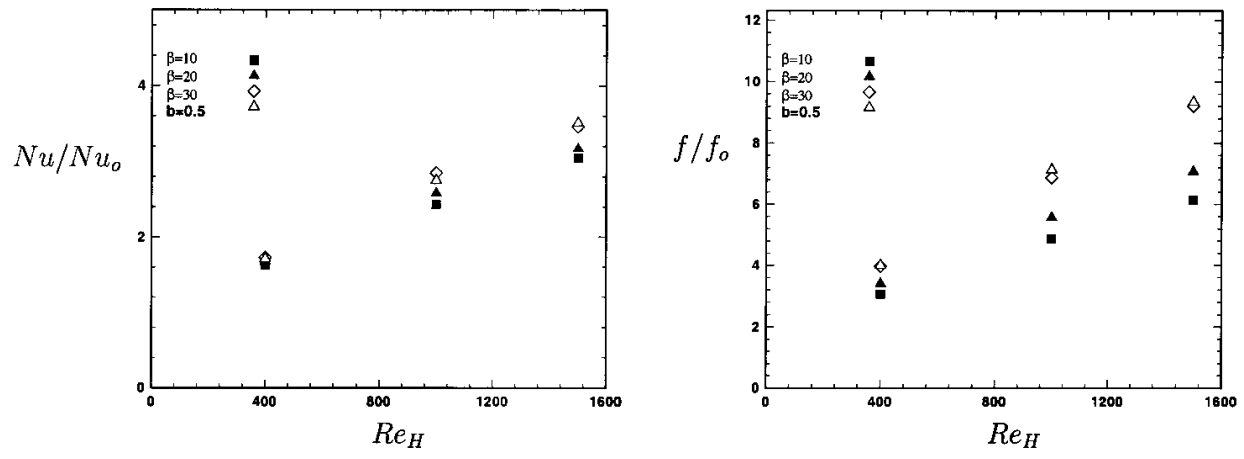

Figure 7. Time- and area-averaged Nusselt number (Nu) and apparent friction factor (f) as a function of Re_H for Cases 1–4. Nu_o (= 3.77) and f_o (= $12/\mathrm{Re}_H$) are the Nusselt number and friction factor for fully developed channel flow, respectively.

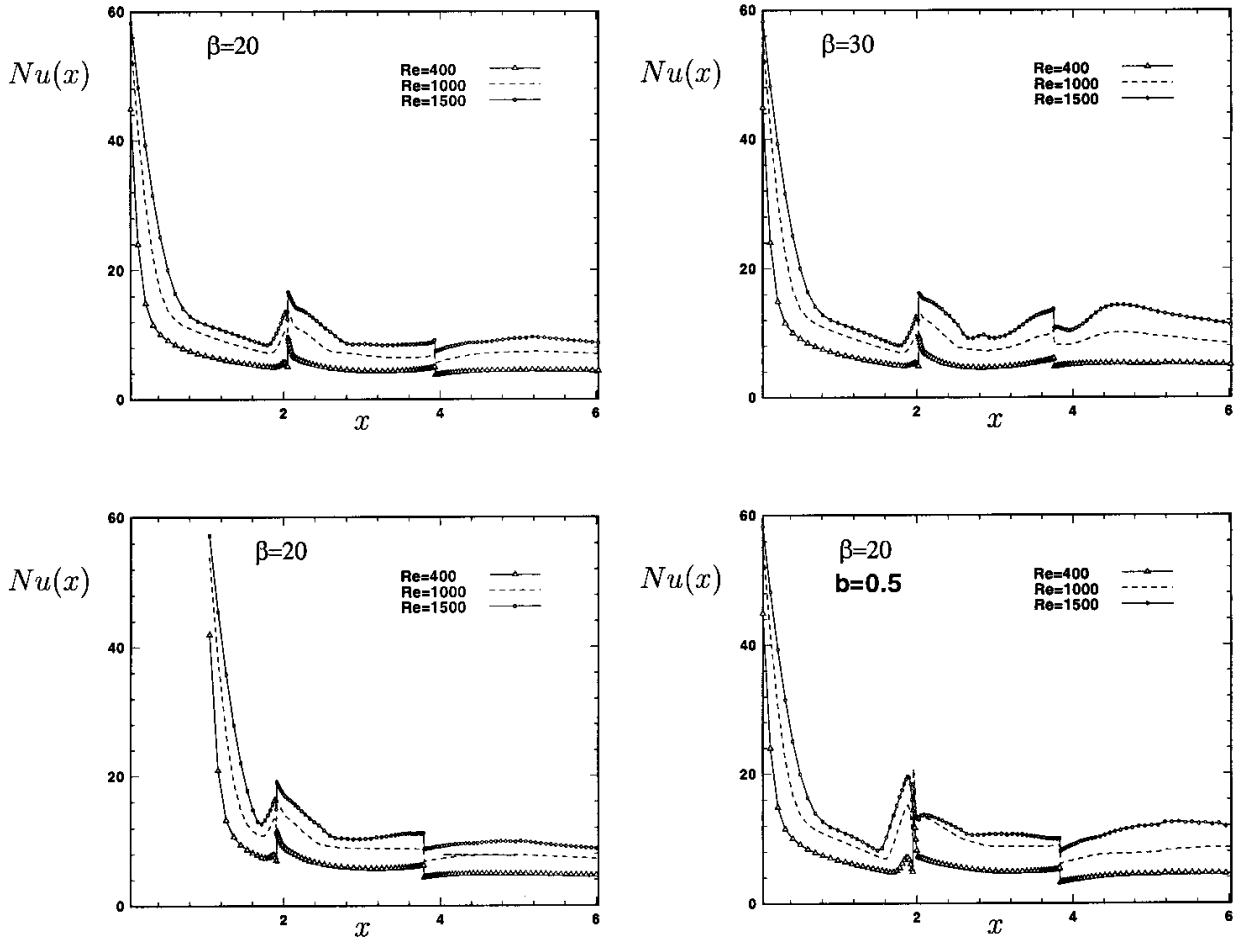

Figure 8. Variation of time- and spanwise-averaged Nusselt number, $\mathrm{Nu}(x)$, in the streamwise direction, Cases 2–5.

$\beta = 30$. In the $\beta = 30$ case, and especially at the higher Reynolds numbers, $\mathrm{Nu}(x)$ first decreases and then increases to a new peak at the end of the VGs.

Figure 9 shows the variations in the cross-sectional time-averaged pressure, $P(x)$ (see Eq. (17)), and bulk temperature, $\theta_b(x)$ (see Eq. (18)), in the streamwise direction for Cases 1–4 at $\mathrm{Re} = 1500$. As is seen in these figures, there are nearly identical results in each case upstream of the VG ($x \leq 2$) for $\theta_b(x)$ and $P(x)$. The bulk temperature, $\theta_b(x)$, increases in the streamwise direction from inlet to outlet. By increasing the angle of incidence from 10° to 30°, the bulk temperature slightly increases and shows similar behavior for all cases. As is expected, the $P(x)$ decreases in the streamwise direction in all the cases, and the pressure drop increases with increasing angles of incidence at each Reynolds number.

Influence of thickness of the VG. In this subsection, the influence of using thicker VG ($b = 0.5$, Case 4) than in the standard case (Case 2), where b is equal to 0.2, is investigated for different Reynolds numbers. From Figure 7, it is observed that Nu and f at each Reynolds number for Case 4 are higher than for Case 2. The difference between the results in these two cases increases with increasing Reynolds numbers. For example, the increase in Nu and f (from Case 2 to Case 4) is 2% and 17%, respectively, at $\mathrm{Re} = 400$, whereas these are

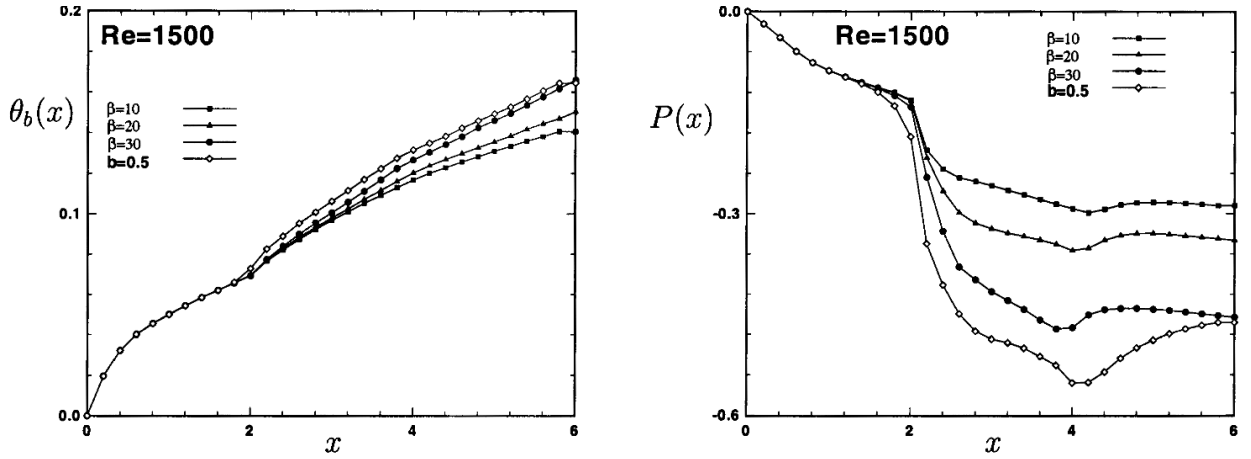

Figure 9. Variation of spanwise-averaged pressure, $P(x)$, and bulk temperature, $\theta_b(x)$, in the streamwise direction for Cases 1–4. $\mathrm{Re} = 1500$.

11% and 32% at $\mathrm{Re} = 1500$. Two major differences are found in these two cases, which result in an increased Nusselt number in Case 4. First, as is seen in Figures 6 and 8, the stagnation region in front of the VGs gives high Nusselt numbers for the thicker VG case (Case 4). Second, stronger and larger streamwise vortices also form, which causes a higher Nusselt number downstream of the VGs.

It can observed in Figure 7 that Nu and f at each Reynolds number for Case 3 ($\beta = 30$, $b = 0.2$) are similar to those in Case 4 ($\beta = 20$, $b = 0.5$). This means that using thicker VGs and a lower angle of incidence works similar to using thin VGs with a higher angle of incidence. In spite of the similarity in the global results for these two cases (Cases 3 and 4), there is a dissimilarity in the local and spanwise-averaged Nusselt numbers. For example, there is a larger peak in front of the VGs in Case 4 as compared with Case 3; see Figure 8.

Influence of Reduction of Upstream Extent. In this subsection, the influence of using a shorter distance between inlet and VGs (Case 5) is investigated. By comparing Nu and f for Cases 2 and 5, it is observed that the predicted Nu and f for Case 5 ($x_o = 1$) are about 11% and 10% higher than the corresponding values for Case 2 ($x_o = 2$). Figure 8 shows the variations of spanwise-averaged Nusselt number for these two cases (Cases 2 and 5). As is seen, the variation in $\mathrm{Nu}(x)$ for different Reynolds numbers is approximately similar. When the larger upstream extent is used, the Nu in the region upstream of the VGs reaches a lower level with a smaller peak at the beginning of the VGs.

CONCLUSIONS

An extensive numerical investigation was made of fluid flow and heat transfer around block-shaped vortex generators at different angles of incidence, which are mounted on one side of a channel for $\mathrm{Re}_H = 400-1500$ and $\mathrm{Pr} = 0.71$. The main conclusions are as follows.

- Time-dependent calculations show that the flow is steady up to $Re_H = 1000$ and that unsteady flow occurs at a higher Reynolds number, $Re_H > 1000$, for all cases in which the convective term was discretized by the central differencing. In contrast, the flow was steady for all Reynolds numbers when the QUICK scheme was used. The reason is that, contrary to the CENTRAL scheme, the QUICK scheme is dissipative. In general, dissipative schemes are designed to damp numerical oscillations. The problem, when simulating transitional flows as in this study, is that dissipative schemes like the QUICK scheme also damp physical oscillations. The conclusion is that dissipative schemes like QUICK should not be used when studying transitional flows.
- This type of VG generates longitudinal vortices behind the VG, which enhance heat transfer locally and globally by their corkscrew motions. These vortices induce a flow toward the heat transfer surface, which enhances the mixing of cold and hot fluid. This downwash secondary flow enhanced the heat transfer.
- The time- and area-averaged Nusselt number, Nu, and friction factor, f, increase at each angle of incidence for increasing Reynolds numbers.
- At each Reynolds number, the time- and area-averaged Nusselt number and friction factor increase for increasing angle of incidence.
- When thicker VGs are used, stronger and bigger streamwise vortices are formed downstream of the VGs, which give rise to a higher Nusselt number.
- Similar global results are found when using thicker VGs with a lower angle of incidence as when using thin VGs with a higher angle of incidence. In spite of the similarity of global results for these two cases, there is dissimilarity in local and spanwise-averaged Nusselt numbers.
- When a larger upstream extent is used, the Nu in the region upstream of the VGs reaches a lower level with a smaller peak at the beginning of the VGs.

REFERENCES

1. R. L. Webb, *Principles of Enhanced Heat Transfer*. John Wiley & Sons, Chichester, UK, 1994.
2. G. Biswas, P. Deb, and N. K. Mitra, Heat Transfer and Flow Structure in Laminar and Turbulent Flows in a Rectangular Channel with Longitudinal Vortices, *International Journal of Heat and Mass Transfer*, vol. 38, pp. 2427–2444, 1995.
3. M. Fiebig, Vortex Generators for Compact Heat Transfer, *J. of Enhanced Heat Transfer*, vol. 2, pp. 43–61, 1995.
4. M. Fiebig, Vortices, Generators and Heat Transfer, *Trans. ICHemE., Part A*, vol. 76, pp. 108–123, 1998.
5. K. N. Atkinson, R. Drakulic, M. R. Heikal, and T. A. Cowell, Two- and Three-Dimensional Numerical Models of Flow and Heat Transfer over Louvred Fin Arrays in Compact Heat Exchangers, *International Journal of Heat and Mass Transfer*, vol. 41, pp. 4063–4080, 1998.

6. N. C. DeJong, L. W. Zhang, A. M. Jacobi, S. Balachander, and D. K. Tafti, A Complementary Experiment and Numerical Study of the Flow and Heat Transfer in Offset Strip-Fin Heat Exchangers, *Trans. ASME: J. Heat Transfer*, vol. 120, pp. 690–698, 1998.
7. L. W. Zhang, D. K. Tafti, and S. Balachander, Computatons of Flow and Heat Transfer in Parallel-Plate Fin Heat Exchangers on the cm-5. *International Journal of Heat and Mass Transfer*, vol. 40, pp. 325–1341, 1997.
8. L. W. Zhang, S. Balachander, D. K. Tafti, and F. M. Najjar, Heat Transfer Enhancement Mechanisms in Inline and Staggered Parallel-Plate fin Heat Exchangers, *International Journal of Heat and Mass Transfer*, vol. 40, pp. 2307–2325, 1997.
9. C. C. Wang, C. J. Lee, C. T. Chang, and S. P. Lin, Heat Transfer and Friction Correlation for Compact Louvered Fin-and-Tube Heat Exchangers, *International Journal of Heat and Mass Transfer*, vol. 42, pp. 1945–1956, 1999.
10. T. A. Rush, T. A. Newell, and A. M. Jacobi, An xperimental Study of Flow and Heat Transfer in Sinusoidal Wavy Passages, *International Journal of Heat and Mass Transfer*, vol. 42, pp. 542–1553, 1999.
11. D. K. Tafti, L. W. Zhang, and G. Wang, Time-Dependent Calculation Procedure for Fully Developed and Developing Flow and Heat Transfer in Louvered Fin Geometries, *Numerical Heat Transfer, Part A*, vol. 35, pp. 225–249, 1999.
12. G. Biswas, N. K. Mitra, and M. Fiebig, Heat Transfer Enhancement in Fin-Tube Heat Exchangers in Winglet Type Vortex Generators, *International Journal of Heat and Mass Transfer*, vol. 28, pp. 282–291, 1994.
13. A. Sohankar, L. Davidson, and C. Norberg, Large Eddy Simulation of Flow Past a Square Cylinder: Comparison of Different Subgrid Scale Models, *Trans. ASME: J. Fluids Engrg.*, vol. 122, no. 1, pp. 39–47, 2000.
14. A. Sohankar, L. Davidson, and C. Norberg, Erratum, *Trans. ASME: J. Fluids Engrg.*, vol. 122, no 3, p. 643, 2000.
15. A. Sohankar, C. Norberg, and L. Davidson, Simulation of Unsteady Three-Dimensional Flow around a Square Cylinder at Moderate Reynolds Numbers, *Phys. Fluids*, vol. 11, no. 2, pp. 288–306, 1999.
16. C. H. K. Williamson, Vortex Dynamics in the Cylinder Wake, *Annual Review of Fluid Mechanics*, vol. 28, pp. 477–539, 1996.
17. A. Sohankar, *Numerical Study of Laminar, Transitional and Turbulent Flow Past Rectangular Cylinders*, Ph.D. thesis, Dept. of Thermo and Fluid Dynamics, Chalmbers University of Technology, Gothenburg, 1998.
18. M. Fiebig, A. Valencia, and N. K. Mitra, Wing-Type Vortex Generators for Fin-and-Tube Heat Exchangers, *Experimental Thermal and Fluid Science*, vol. 7, pp. 287–295, 1993.
19. M. Fiebig, Vortices and Heat Transfer, *ZAMM*, vol. 77, pp. 3–18, 1997.
20. L. Davison, LES of Recirculating Flow without Any Homogeneous Direction: A Dynamic One-Equation Subgrid Model. In *2nd Int. Symp. on Turbulence Heat and Mass Transfer*, pp. 481–490, Delft, 1997.
21. P. Emvin, *The full Multigrid Method Applied to Turbulent Flow in Ventilated Enclosures Using Structured and Unstructured Grids*, Ph.D. thesis, Dept. of Thermo and Fluid Dynamics, Chalmbers University of Technology, Gothenburg, 1997.
22. A. G. Kravenchenko and P. Moin, Numerical Studies of Flow over a Circular Cylinder at $re_d = 3900$, *Phys. Fluids A*, vol. 12, no. 2, pp. 403–417, 2000.
23. M. Breuer, Large Eddy Simulation if the Subcritical Flow Past a Circular Cylinder: Numerical and Modeling Aspects, *Int. J. Num. Meth. Fluids*, vol. 28, pp. 1281–1302, 1998.
24. G. Biswas, K. Toril, D. Fujii, and K. Nishino, Numerical and Experimental Determination of Flow Structure and Heat Transfer Effects of Longitudinal Vortices in a Channel Flow, *International Journal of Heat and Mass Transfer*, vol. 39, pp. 3441–3451, 1996.